Materials Advances

ROYAL SOCIETY OF CHEMISTRY

PAPER

View Article Online
View Journal

Cite this: DOI: 10.1039/d5ma01066g

Fluoride-assisted hydroxyl reduction in Er^{3+}-doped tellurite glass and amorphous thin films for enhanced optical and spectroscopic performances

Pradeep Ramanan, *[ad] Florent Starecki,[bc] Jan Gutwirth, [d] Virginie Nazabal, [cd] Matthieu Roussey,[e] Petr Němec *[d] and Laeticia Petit[a]

Received 16th September 2025,
Accepted 11th January 2026

DOI: 10.1039/d5ma01066g

rsc.li/materials-advances

Tellurite glass with the composition 68.25 TeO_2–19.5 ZnO–9.75 Bi_2O_3–2.5 Er_2O_3 (in mol%) is a promising material for integrated photonics. However, the emission efficiency of erbium ions in the glass host is constrained by the strong absorption of hydroxyl groups present in the glass. To counteract these losses arising from hydroxyl groups, ammonium bifluoride as a dehydrating agent is added to the glass batch before melting and its impact not only on the optical, thermal, structural, and spectroscopic properties of the glass but also on the properties of amorphous thin films is examined. A reduction in hydroxyl group concentration is confirmed in the bulk, leading to an enhancement in the glass spectroscopic properties. However, residual fluorine originating from the ammonium bifluoride remains in the glass. While the presence of fluorine in the glass target has minimal impact on the deposition process itself, fluorine is also found in the film, resulting in a film with a lower refractive index than initially targeted. Nevertheless, the films deposited from the dehydrated glass target are seen to exhibit similar properties close to those of films from a non-dehydrated target.

1. Introduction

Rare-earth doped glasses, particularly those incorporating erbium ions (Er^{3+}), play a crucial role in photonics, especially in optical amplification and telecommunications.[1] Their significance stems from the characteristic emission of Er^{3+}, centred around 1.5 μm, resulting from the $^4I_{13/2} \rightarrow {}^4I_{15/2}$ transition. This emission precisely aligns with the conventional (C) band in the short-wave infrared spectrum.[2] As a result, Er^{3+}-doped materials have been utilized for signal amplification in waveguides,[3,4] photonic integrated circuits,[5] and LIDAR systems,[6,7] just to cite a few.

Tellurite-based glasses have emerged as exceptional host materials for rare-earth dopants, particularly for Er^{3+}.[8] Unlike conventional silica or phosphate glasses, tellurite glasses exhibit high refractive indices (RIs) (1.9–2.2 at 632 nm depending on the glass composition).[9,10] Their relatively low phonon energy ($\leq$800 cm^{-1}) and excellent transparency (~400 nm to ~6 μm depending on the glass composition)[11] make them ideal for photonic applications.[12] Their intrinsically low phonon energy for oxide glasses lowers the non-radiative processes, thereby enhancing the efficiency of emission from the rare-earth ions, boosting the efficiency of optical amplification in both bulk and thin film configurations. Tellurite glasses offer excellent thermal and chemical stability, allowing for reliable operation in harsh environments. Their ability to accommodate high concentrations of Er^{3+} without excessive clustering ensures uniform doping[13] and makes them highly suitable for next-generation photonic circuits[5] and medical laser applications.[14]

Because pure tellurite glass cannot be vitrified using the conventional melt-quenching technique, tellurite glasses are typically formulated as multi-component materials.[15] For example, ZnO can be added to improve both the glass-forming ability and mechanical durability,[16–18] while the incorporation of Bi_2O_3 can increase the refractive index and glass chemical durability while simultaneously lowering phonon energy, all of which contribute to improved luminescence efficiency.[19]

Therefore, numerous studies have explored the optical and structural properties of tellurite glasses, especially within the TeO_2–Bi_2O_3–ZnO system, highlighting their potential for photonic applications.[20,21] Lemiere *et al.* demonstrated strong emissions centred at 1.5 and 2.7 μm from the glass with the

[a] *Photonics Laboratory, Tampere University, Korkeakoulunkatu 3, Tampere, 33720, Finland. E-mail: pradeep.ramanan@tuni.fi*
[b] *École nationale supérieure d'ingénieurs de Caen (ENSICAEN), Research Center on Ions, Materials and Photonics (CIMAP), Caen 14000, France*
[c] *Institut des Sciences Chimiques de Rennes (ISCR), Univ Rennes, CNRS – UMR 6226, F-35000 Rennes, France*
[d] *Faculty of Chemical Technology, University of Pardubice, Studentská 573, 532 10 Pardubice, Czech Republic. E-mail: petr.nemec@upce.cz*
[e] *Centre for Photonics Sciences, University of Eastern Finland, P.O. Box 111, 80101 Joensuu, Finland*

composition 68.25 TeO_2–19.5 ZnO–9.75 Bi_2O_3–2.5 Er_2O_3 (in mol%).[22] Recently, a successful amorphous thin films' deposition from this glass was demonstrated using radio frequency (rf)-magnetron sputtering, suggesting that it is well-suited for telecommunication devices.[23]

However, the presence of hydroxyl (OH) groups in Er^{3+}-doped glasses and amorphous thin films poses a significant challenge to their optical performance, particularly in photonic and laser applications. Indeed, OH groups are recognized as effective luminescence quenchers for Er^{3+} ions,[24] especially at the key telecommunication wavelength (C-band).[25] This effect leads to lower fluorescence lifetimes, increased signal attenuation, and diminished optical amplification efficiency, making OH reduction a crucial aspect of material optimization. There has been research focusing on bulk glass synthesis by refining the synthesis methods, incorporating dehydration treatments, and optimizing precursor compositions to minimize OH impurities.[26,27] Massera *et al.*[28] demonstrated the extent of dehydration possible in the TeO_2–ZnO–Bi_2O_3 glass system, highlighting the effectiveness of using ammonium bifluoride (NH_4F–HF) as the dehydrating agent while also emphasizing the influence of pure oxygen atmosphere and substitutional use of halide precursors in place of oxide chemicals.

In this study, tellurite glasses are prepared by adding NH_4F–HF into the glass batch. We examine the influence of NH_4F–HF as a dehydrating agent, particularly in relation to the thermal, optical and spectroscopic properties of glass as well as to the optical quality of films.

2. Methods and materials

2.1 Target preparation and film deposition

Tellurite glasses with the composition 68.25 TeO_2–19.5 ZnO–9.75 Bi_2O_3–2.5 Er_2O_3 (in mol%) were synthesized using tellurium(IV) oxide (Thermo Scientific, 99%), zinc oxide (Thermo Scientific, 99%), bismuth(III) oxide (Thermo Scientific, 99%) and erbium(III) oxide (Thermo Scientific 99.9%). The glasses were prepared using the standard melt quench technique under an ambient atmosphere. NH_4F–HF (Thermo Scientific, 95%) was added into the parent glass batch up to 4 wt% (x = 0, 1, 2, 3 and 4 wt%). Before melting, the 10 g batches were pretreated at 600 °C for 1 h to allow the reaction of NH_4F–HF with the glass batch and then melted in a platinum crucible at 775 °C for 3.5 h. After quenching, the glasses were annealed at 300 °C for 6 h.

A large batch of 60 g was also melted from the glass prepared with x = 4 using the same procedure and cast into a cylindrical 2″ mold to obtain a glass target with the desired shape required for sputtering (labelled as x = 4 (LB)). After annealing, the glass disk was surface ground to achieve ~3.5 mm thickness and flat parallel surfaces using a bench-top polisher (PM5 Precision Lapping & Polishing system, Logitech) as in ref. 23.

Deposition of thin films from the 2″ glass (x = 4 (LB)) disk used as the target was carried out using (rf)-magnetron sputtering in a multichamber deposition system (MPE600S, Plassys Bestek). The sputtering power was 20 W and the argon : oxygen ($Ar : O_2$) gas flow ratio 40 : 10 sccm. The chamber was maintained at an overall pressure of 5×10^{-3} mbars during the deposition process. The substrates were placed face to face above the target, 50 mm apart and rotated at 5 rpm. Film depositions were performed on p-type crystalline silicon (Si) ⟨100⟩ wafers, 2″ oxidized Si (SiO_2/Si) wafers and N-BK7 glass (Schott).

2.2 Characterization

X-ray diffraction (XRD) analysis was performed for both bulk glasses (crushed and powdered) and films deposited on a BK7 substrate using an X-ray diffractometer (PANalytical Empyrean) under a Cu K_α line with a 99 s step time and 0.026° step size for 2θ ranging from 10° to 90°.

Glass density was measured based on the Archimedes principle using a precision balance (Adventurer AX124/E, Ohaus Corporation) with ethanol as the immersion liquid and with a 0.02 g cm^{-3} accuracy.

The Raman spectra of the bulk glasses were obtained under a 785 nm excitation using a micro-Raman system (inVia Raman microscope, Renishaw) consisting of a 50× long microscope objective and 1200 lines per mm grating. A 100 s exposure time and 10 scan accumulation were used with the power being kept at 0.05% (3.925 mW) to minimize the luminescence signal from Er^{3+}.

The infrared (IR) absorption spectra were obtained using a Fourier Transform Infrared (FTIR) spectrometer (L1600300 Spectrum TWO LiTa, PerkinElmer) from 600 cm^{-1} to 4000 cm^{-1} with a 4 cm^{-1} resolution and 4-scan average.

The composition of the glasses was analysed using an Electron Probe MicroAnalyzer (EPMA) (CAMECA, SX100) equipped with 5 wavelength dispersive X-ray analysers (WDX). The EPMA was operated at 15 keV and 40 nA. Quantitative analyses were performed using the Cameca QUANTITOOL analytical program, calibrated with the ErF_3 reference standard, applying a PAP matrix correction. The samples were polished and were immediately coated with a carbon layer to prevent charging. For obtaining the films and sputtering target composition and the images of the films' surface, a scanning electron microscope (SEM) (LYRA 3, Tescan) equipped with an Energy Dispersive Spectroscopy (EDS) analyser (Aztec X-Max 20, Oxford Instruments) was used. 10 keV acceleration voltage was used, and the analysis was performed using the Aztec software provided by Oxford Instruments. Both the films and sputtering targets were carbon-coated (using Leica ACE200) to mitigate charge buildup.

Differential scanning calorimetry (DSC) was carried out using a thermogravimetric analyser (STA 449 F1 Jupiter, Netzsch) in a platinum–rhodium crucible at a heating rate of 10 °C min^{-1}. The inflection point in the first endotherm of the DSC curve was used for determining the glass transition temperature (T_g). The onset and peak of the first exotherm were taken as the crystallization onset temperature (T_x) and crystallization temperature (T_p).

The UV-VIS-NIR absorption spectrum of the glasses and the transmission spectrum of the films deposited on the BK7

substrate were obtained using a UV-VIS-NIR spectrometer (LAMBDA 1050+, PerkinElmer) at a step resolution of 1 nm for a wavelength range of 1700–250 nm and 2300–250 nm, respectively. The absorption cross-section (σ_{abs}) at the wavelength of interest was calculated with an accuracy of ±10% using the relation in ref. 22.

The refractive index (RI) of the bulks was measured at 6 wavelengths (443, 635, 854, 1064, 1302, and 1540 nm) using a prism coupler (Model 2010/M, Metricon Corporation). The RI experimental data were fitted using Sellmeier's equation.

Variable angle spectroscopic ellipsometry (VASE) was used to estimate the thickness and RI of the deposited films. A rotating analyser ellipsometer (VASE, J. A. Woollam) at an angle of incidence from 50° to 70° in 10° increments over a wavelength range of 280–2300 nm was used to perform the measurement. As in ref. 23, the VASE data of thin films were fitted using the Cody–Lorentz model.[29] The RI dispersion of the thin films was also measured in the 2300–20 000 nm range using a second ellipsometer (IR-VASE, J. A. Woollam) with a 16 cm^{-1} resolution and was fitted using the Gaussian oscillator model[30,31] and the WVASE software.

The upconversion (UC) spectra as well as the emission spectra centred at 1.5 and 2.7 μm were measured from glasses crushed into powder, using a continuous-wave (CW) 976 nm monochromatic single-mode fibre-pigtailed laser diode (CM962UF76P-10R, Oclaro) as the excitation. The setup included a custom optical bench layout with a photomultiplier tube and Indium Gallium Arsenide (InGaAs) detector (SPECTRO 320 Scanning Spectrometer, Instrument Systems Konica Minolta) for the visible and near-IR (NIR) range. For mid-IR (MIR), a lock-in amplifier (SR830, Standford Research Systems), an optical chopper (SR540, Standford Research Systems), a transimpedance amplifier, and a detector (PIP-DC-200M-F-M4, PVI-4TE-4-1 ×1, Vigo Photonics) were used. The step resolution for all measurements was 1 nm. The lifetime of the $^4I_{13/2}$ level of Er^{3+} was measured using the 976 nm laser source (BL976-PAG700, Thorlabs) mounted on a pulsed laser diode driver and an integrated TEC controller (CC-S, AlphaNov) with the output from the InGaAs detector (PDA10CS2, Thorlabs) being handled with an oscilloscope (PicoScope 5000D Series, Pico Technology Ltd). A 32-scan average was selected during data acquisition.

The NIR luminescence spectra of the thin films were measured using a 976 nm laser diode (Q-Photonics QSP-975-10), with an incident power of 8 W. The emission spectra were acquired with a liquid nitrogen cooled InGaAs detector, and lifetimes with a thermoelectrically cooled InGaAs equipped with an amplifier of a higher bandwidth (3.5 MHz). A long-pass filter was used to isolate the 1.55 μm transition (Thorlabs FEL-1100).

Surface roughness of the deposited films was mapped through atomic force microscopy (AFM) for an area of 5 × 5 μm^2 and 512-line scan resolution. A single-crystal Si tip (HA_NC, ScanSens GmbH) having a force constant of 12 N m^{-1} and a resonant frequency of 235 kHz was used in the scanning probe microscope (Ntegra Academia, Nt-MDT) in semi-contact mode.

3. Results and discussion

Er^{3+} doped tellurite glasses with the composition 68.25 TeO_2–19.5 ZnO–9.75 Bi_2O_3–2.5 Er_2O_3 (in mol%) were prepared with NH_4F–HF in order to reduce their OH content, similar to one of the approaches performed in ref. 28. In the current study, the addition of NH_4F–HF to the glass batch beyond 4 wt% was not possible due to the occurrence of crystallization while quenching the glass. The amorphous nature of the investigated glasses was confirmed from XRD patterns (shown in SI Fig. S1(a)).

3.1 Target preparation and characterization

Fig. 1 shows the IR absorption spectra of the investigated glasses, which show a broad absorption band between ~2500 and 3500 cm^{-1}. This band is attributed to the free OH group "weakly associated" at 3500 cm^{-1} and to OH groups which are "strongly associated" at around 2800 cm^{-1}.[26] The spectra also show an absorption centred at ~2250 cm^{-1}, which can be attributed to the "very strongly associated" OH groups. The band at 2250 cm^{-1} could also be interpreted as the second overtone of the fundamental band at 1125 cm^{-1}, which is typically assigned to OH bending or stretching modes in the glass matrix.[32] As expected, an increase in the concentration of NH_4F–HF from 0 to 4 wt% leads to a decrease in intensity of the bands, confirming the decrease in the concentration of the OH groups, the lowest amount being for the glass with x = 4. Indeed, NH_4F–HF is known to react with OH groups bound to tellurium (Te) and results in the evolution of hydrogen fluoride (HF) gas.[33,34]

The incorporation of NH_4F–HF in the glass batch before melting influences various glass properties, such as the thermal properties of the glasses, as illustrated in Fig. 2(a) and summarized in Table 1.

With increasing x, the glass transition temperature (T_g) progressively decreases. The glass with x = 0 exhibits an

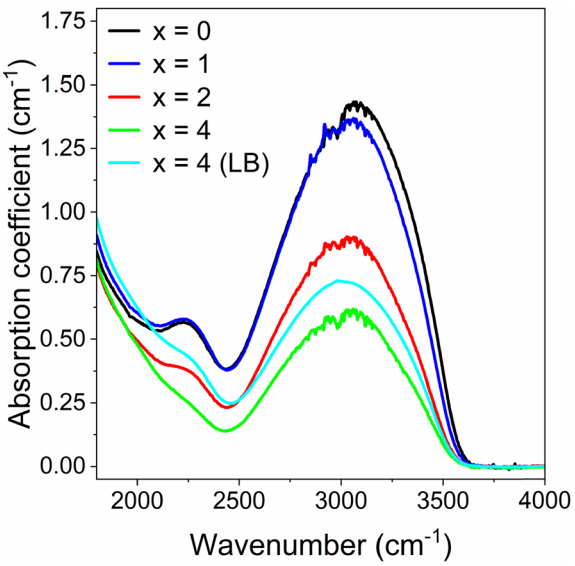

Fig. 1 FTIR spectra of the investigated glasses.

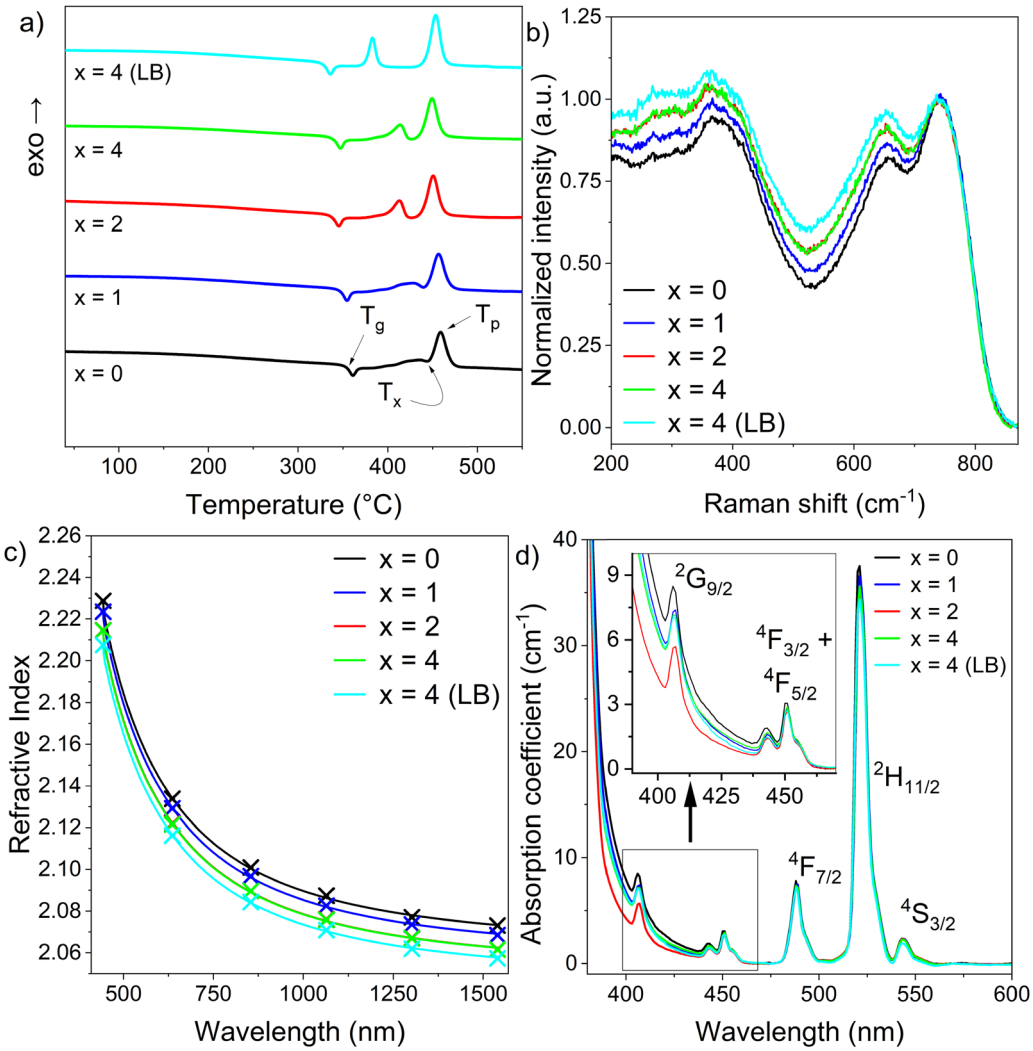

Fig. 2 (a) DSC thermograms, (b) normalized Raman spectra at ~745 cm^{-1} obtained using 785 nm excitation, (c) RI dispersion curves (x = 4 overlaps with x = 2), and (d) absorption spectra of the glasses in the UV-visible region (inset details region of $^4I_{15/2}$ → $^4F_{3/2}$, $^4F_{5/2}$ and $^2G_{9/2}$ transitions).

exothermic peak at 435 ± 3 °C. As x increases, a second exothermic peak emerges, shifting the first exothermic peak towards lower temperatures. The crystallization temperature decreases more rapidly than T_g, slightly affecting the thermal stability window (ΔT). As x increases, the glasses become more prone to crystallization, reducing their ability to remain amorphous under thermal exposure. As shown in Table 1, all glasses exhibit similar density.

In order to understand the changes in the thermal properties, the chemical composition of the glasses was analysed. Residual fluorine (F) was detected in the glasses, and its concentration increased as the wt% of NH_4F–HF was increased from 0 to 4 (Table 2). It is the residual F in the glass network which is suspected to weaken the overall glass network by breaking Te–O bonds and forming Te–F bonds, leading to

Table 1 Physical and thermal properties of synthesized glasses

Glass	ρ (g cm^{-3}) ± 0.02	T_g (°C) ± 3	T_x (°C) ± 3	T_p (°C) ± 3	$\Delta T = T_x - T_g$ (°C) ± 6
x = 0	6.26	358	409	435	51
x = 1	6.28	352	402	428	50
x = 2	6.27	342	402	413	60
x = 4	6.28	344	401	414	57
x = 4 (LB)	6.24	334	375	383	41

Table 2 Chemical composition analysis of the investigated glasses performed using EPMA

Glass	O (at%) ± 1	F (at%) ± 1	Zn (at%) ± 1	Te (at%) ± 1	Er (at%) ± 1	Bi (at%) ± 1
Theoretical	63	—	6	22	2	6
x = 0	62	—	7	23	2	7
x = 1	62	1	7	23	2	6
x = 2	60	2	7	23	2	6
x = 4	60	3	7	23	2	6
x = 4 (LB)	59	4	7	22	2	6

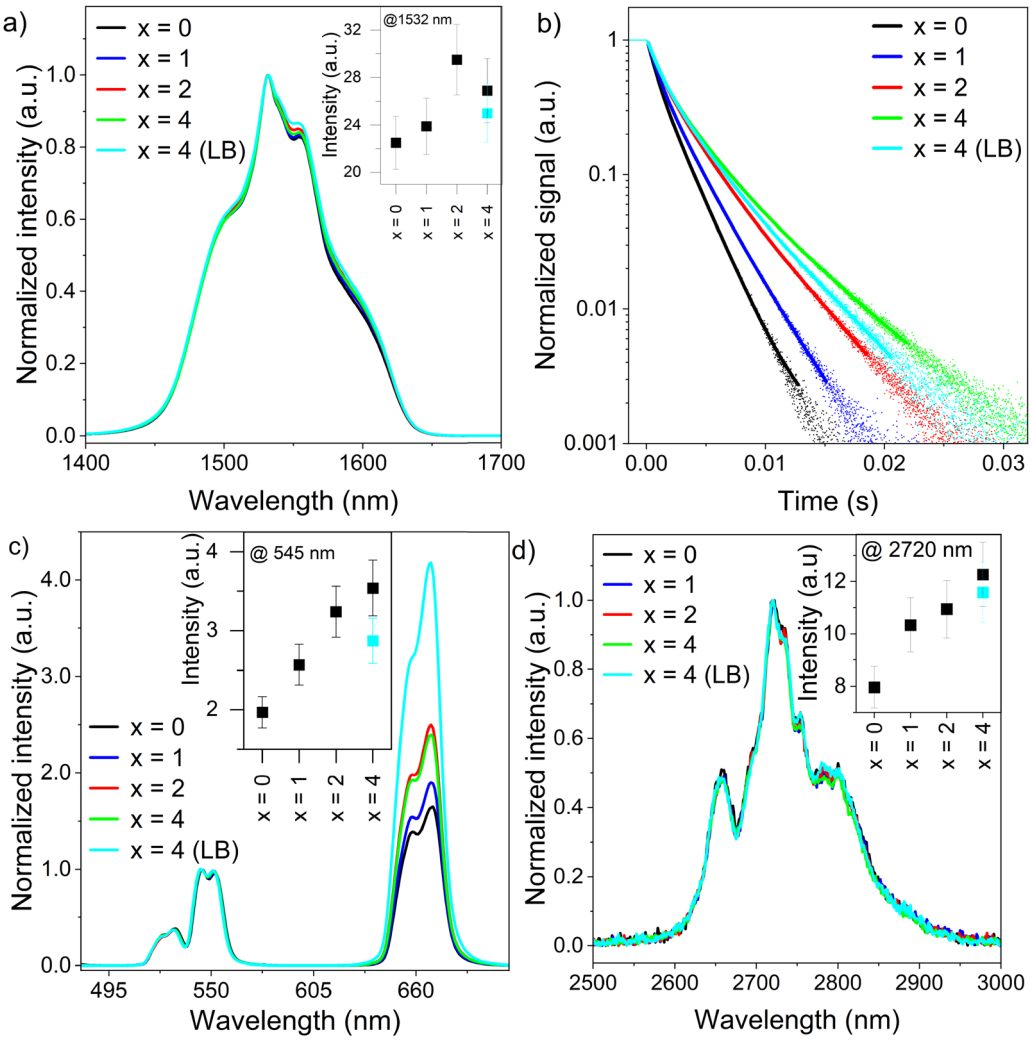

Fig. 3 (a) Normalized NIR emission spectra at 1620 nm (inset shows the intensity of the emission at 1532 nm as a function of *x*), (b) emission decay curves for the $^4I_{13/2} \rightarrow {}^4I_{15/2}$ transition of Er^{3+} and their corresponding fits, (c) normalized UC spectra (inset shows the intensity of the emission at 545 nm as a function of *x*), (d) normalized MIR emission spectra at 2720 nm (inset shows the intensity of the emission at 2720 nm as a function of *x*). All data were obtained using an excitation at 976 nm.

reduced thermal stability and a lower T_g, in agreement with ref. 35.

The residual F in the glass also has a noticeable impact on the structure of the glasses, as shown in Fig. 2(b), which presents the normalized Raman spectra of the glasses. The Raman band in the 350–550 cm^{-1} range is associated with symmetrical bending vibrations of Te–O–Te bonds and the Zn–O–Zn/Te bridges.[36,37] The band centred at around ~664 cm^{-1} corresponds to the symmetrical stretching of TeO_4 units and the asymmetric Te–O bond stretching, while the ~745 cm^{-1} band is attributed to the symmetric stretching of TeO_3 and TeO_{3+1} units.[38,39] An increase in *x* is suspected to lead to an increase in the intensity of the band at ~664 cm^{-1} compared to the band at ~745 cm^{-1}, suggesting a larger number of TeO_4 units at the expense of $TeO_{3/3+1}$ units in the glasses prepared with a large amount of NH_4F–HF.

Furthermore, the addition of NH_4F–HF also has a noticeable impact on the RI of the glasses as shown in Fig. 2(c). An increase in *x* decreases the RIs. As polymerization increases, more Te–O–Te linkages form, creating a denser glass structure. Even though this higher connectivity reduces the number of non-bridging oxygens in the TeO_4 units, residual F present in the $TeO_{3/3+1}$ units leads to decreased electronic polarizability, which contributes to decreasing the RI of the glass. Therefore, the decrease in RI with an increase in *x* must be related to the residual F in the glasses. Due to the removal of oxygen, the replacement of F in the glass network reduces the polarizability and so the RI of the glass is in agreement with former studies.[40,41]

The absorption spectra in the UV-visible spectral region shown in Fig. 2(d) display the typical absorption bands of Er^{3+} ions, which correspond to the 4f–4f transitions of Er^{3+} from the ground state ($^4I_{15/2}$) to the different excited states.[42] An increase in *x* leads to a small shift of the optical band gap to a lower wavelength in agreement with the decrease in the RI seen with an increase in *x* (Fig. 2(c)). Within the accuracy of the measurement (±10%), the absorption cross-section and

Table 3 Fitting parameters and calculated average lifetime for the $^4I_{13/2} \rightarrow {}^4I_{15/2}$ transition of Er^{3+}

Glass	A_1	τ_1 (ms)	A_2	τ_2 (ms)	Coefficient of determination (R^2)	Average lifetime ± 0.2 (ms)
$x = 0$	0.476	0.84	0.557	2.27	0.99993	1.9
$x = 1$	0.463	0.95	0.567	2.75	0.99995	2.4
$x = 2$	0.482	1.18	0.544	3.63	0.99995	3.1
$x = 4$	0.505	1.15	0.514	4.26	0.99993	3.6
$x = 4$ (LB)	0.512	1.25	0.510	4.01	0.99995	3.4

absorption coefficient at 980 nm and 1532 nm remain unchanged regardless of the NH_4F–HF concentration (shown in SI Fig. S2(a) and (b)). The absorption cross-sections at 980 nm (2.87×10^{-21} cm^2) and 1530 nm (8.78×10^{-21} cm^2) are similar to those reported for other tellurite glasses.[22,43–45]

As expected, the decrease in the OH content has a positive impact on the spectroscopic properties of the glasses, which are presented in Fig. 3.

Fig. 3(a) depicts the normalized NIR emission spectra of the investigated glasses. Since there are some reabsorptions from Er^{3+}, the spectra are normalized at 1620 nm. The characteristic emission band of Er^{3+} in amorphous sites is observed, and this band is due to the $^4I_{13/2} \rightarrow {}^4I_{15/2}$ transition. There is an increase in the intensity of the emission centred at 1.5 μm (shown in the inset) when the concentration of NH_4F–HF is increased. Fig. 3(b) depicts the emission decay curves for the $^4I_{13/2} \rightarrow {}^4I_{15/2}$ transition of Er^{3+} ($\lambda_{exc} = 976$ nm). A biexponential fit, given by (1), was found to capture the decay behaviour better compared to other models, such as for example, Inokuti–Hirayama, single exponential and stretched exponential, suggesting multiple pathways or interactions influencing the excited state lifetime of Er^{3+}.[46]

$$I(t) = A_1 e^{\left(\frac{-t}{\tau_1}\right)} + A_2 e^{\left(\frac{-t}{\tau_2}\right)} \quad (1)$$

A_1 and A_2 are the decay constraints and τ_1 and τ_2 are the first and second lifetime terms, respectively. As summarized in Table 3, an increase in the NH_4F–HF content leads to an increase in the average Er^{3+} $^4I_{13/2}$ excited state lifetime (τ), calculated using (2), which is in agreement with the increase in the NIR emission intensity seen in Fig. 3(a).

$$\tau = \frac{A_1\tau_1^2 + A_2\tau_2^2}{A_1\tau_1 + A_2\tau_2} \quad (2)$$

The OH group is known to act as a strong luminescence quencher, especially at this $^4I_{13/2} \rightarrow {}^4I_{15/2}$ transition.[25] Thus, a reduction in the OH group content is expected to increase the intensity of the emission at 1.5 μm.[47] The increase in the intensity of the emission at 1.5 μm can also be attributed to the structural modifications, as variations in the tellurite network polymerization can affect the local symmetry of Er^{3+} sites. However, a more disrupted network with lower polymerization is believed to increase the asymmetry of Er^{3+} coordination, which may enhance specific spectroscopic features, such as the $^4I_{13/2} \rightarrow {}^4I_{15/2}$ emission.[48] Consequently, the observed increase in the intensity of the emission at 1.5 μm in Fig. 3(a) can primarily be related to the reduction in OH groups, as the glasses exhibiting the strongest emission are the glasses with the most polymerized network.

The UC spectra normalized to the emission band at 545 nm are shown in Fig. 3(c). The spectra exhibit a band at ~530 nm, which can be attributed to $^2H_{11/2} \rightarrow {}^4I_{15/2}$ of Er^{3+} and a band at ~545 nm, which can be assigned to $^4S_{3/2} \rightarrow {}^4I_{15/2}$ of Er^{3+}. The spectra also show a band at ~668 nm, which is due to the $^4F_{9/2} \rightarrow {}^4I_{15/2}$ transition of Er^{3+}. An increase in red UC intensity compared to the green one is observed when the amount of NH_4F–HF is increased from 0 to 4 wt%, indicating that the reduction in OH groups leads to changes in the UC process, especially in the non-radiative relaxation pathways. As depicted in Fig. 4, under ~980 nm laser diode pumping, electrons in the $^4I_{15/2}$ level undergo ground state absorption to transition to the $^4I_{11/2}$ level. From this excited level, they are further excited to the $^4F_{7/2}$ level either through excited state absorption or energy transfer UC ($^4I_{11/2} + {}^4I_{11/2} \rightarrow {}^4I_{15/2} + {}^4F_{7/2}$). The electrons in the $^4F_{7/2}$ level then decay non radiatively to the lower $^2H_{11/2}$ and $^4S_{3/2}$ levels, with the radiative transitions $^2H_{11/2} \rightarrow {}^4I_{15/2}$ and $^4S_{3/2} \rightarrow {}^4I_{15/2}$ resulting in the green emission. As mentioned above, the red emission originates from the $^4F_{9/2} \rightarrow {}^4I_{15/2}$ transition. The electrons at the $^4I_{13/2}$ level can be promoted to the $^4F_{9/2}$ level through excited state absorption or they can reach the $^4F_{9/2}$ level *via* nonradiative decay from the $^4S_{3/2}$ level. From the Er^{3+} energy level diagram, it is evident that electrons in $^4F_{7/2}$ and $^4F_{9/2}$ states are primarily influenced by populations in $^4I_{11/2}$ and $^4I_{13/2}$ levels, respectively. At high OH concentrations, a significant portion of the excitation energy is dissipated as heat—rather than converted to emission.[26] As the OH content decreases, this vibrational quenching is minimized, allowing more energy to remain in the excited states. However,

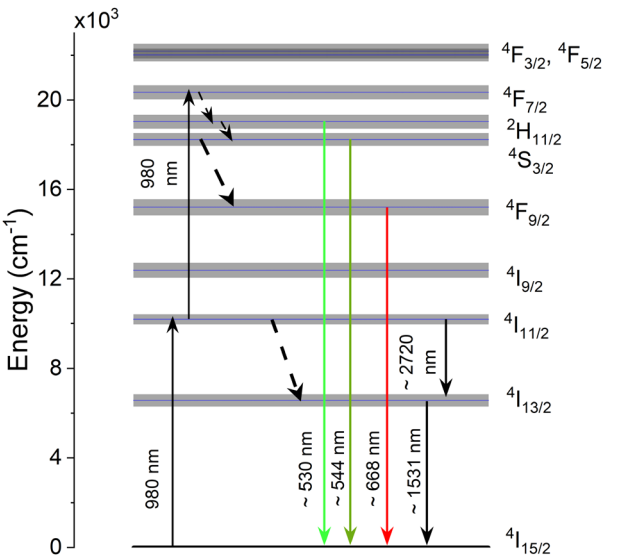

Fig. 4 A simplified 4f–4f energy level diagram of Er^{3+} depicting 980 nm photon absorption, radiative emissions (downward facing solid arrows) and non-radiative emissions (downward facing dashed arrows).

Table 4 Chemical composition analysis of the films performed using EDS

Glass	O (at%) ± 1	F (at%) ± 1	Zn (at%) ± 1	Te (at%) ± 1	Er (at%) ± 1	Bi (at%) ± 1
x = 0 (LB)						
Target	62	—	7	22	2	7
Film	65	—	8	13	3	11
x = 4 (LB)						
Target	58	4	8	22	2	6
Film	64	2	7	16	1	9

the reduction in quenching shifts the energy transfer dynamics toward red-emitting transitions. The $^4F_{9/2}$ level, responsible for the red emission, experiences increased population due to cross-relaxation between Er^{3+} ions and the suppression of non-radiative losses from the green-emitting states. As a result, red UC emission becomes more dominant.[49]

Fig. 3(d) displays the normalized MIR emission spectrum of the investigated glasses at around 2.7 μm. The broad emission band is attributed to the Er^{3+} $^4I_{11/2} \rightarrow {}^4I_{13/2}$ intermediate level transition and its shape remains unchanged as x increases. However, its emission intensity increases as the amount of NH_4F–HF increases due to the reduction in the content of the OH groups as reported in ref. 50 and 51. The 976 nm excitation results in ground state absorption from $^4I_{15/2} \rightarrow {}^4I_{11/2}$. Since the content of OH groups is reduced due to dehydration, the multi-phonon relaxation is lowered, thereby increasing the emission intensity from $^4I_{11/2} \rightarrow {}^4I_{13/2}$.

Because of its low OH content and promising spectroscopic properties, the glass with x = 4 was selected for thin films' deposition. The batch size was scaled up from 10 g to 60 g to allow the preparation of a 2″ glass disk with a thickness of ~3.5 mm. Characterizing the glass (x = 4 (LB)) when changing batch size is essential to ensure consistency and reproducibility, particularly when transitioning from small-scale composition optimization to large-scale sputtering target fabrication. The 2″ glass disk (x = 4 (LB)) was found to have a slightly higher OH content (Fig. 1) and higher F content (Table 2) than the glass prepared from a 10 g batch (x = 4). This resulted in the preparation of a 2″ glass disk with a lower T_g, T_x and

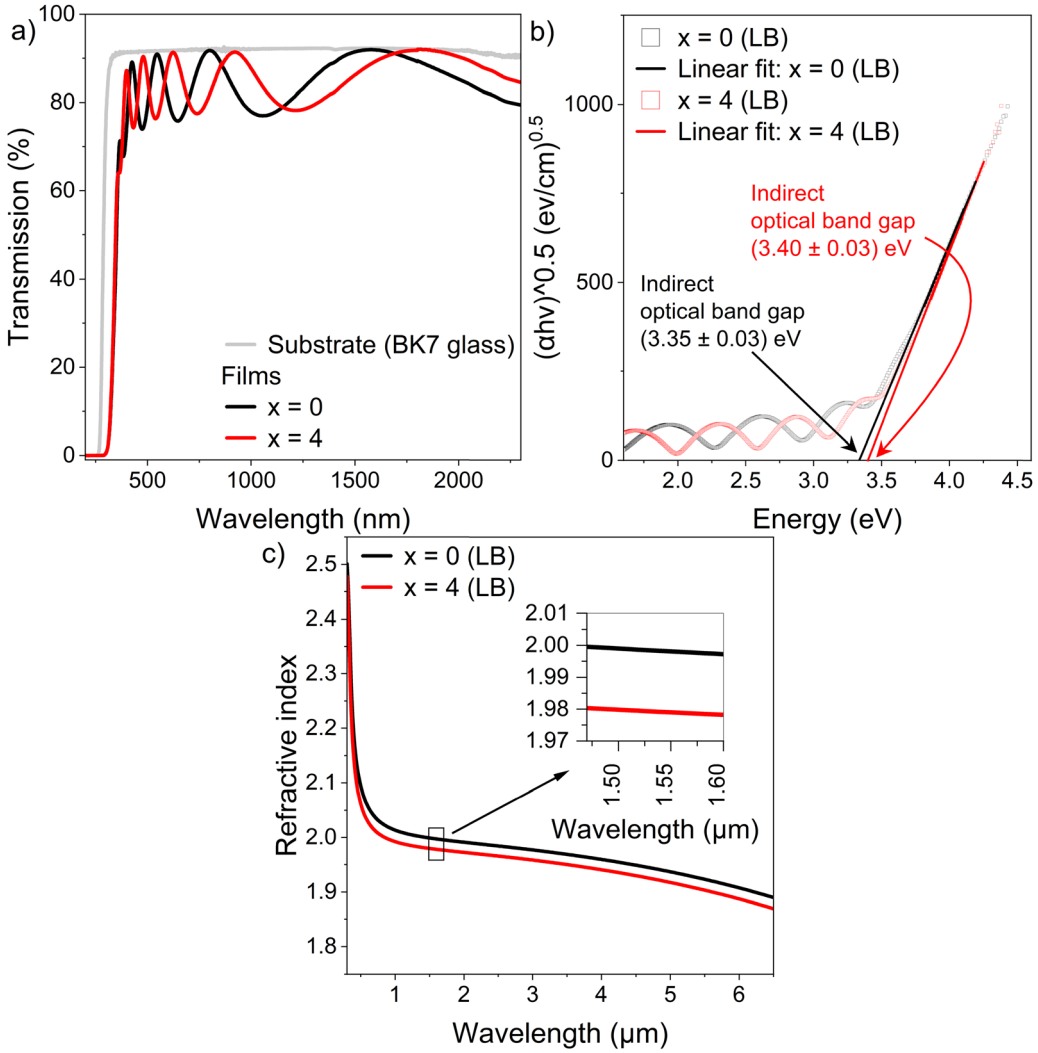

Fig. 5 (a) UV-VIS-NIR transmission spectra, (b) Tauc plots for an indirect allowed transition and (c) RI dispersion curves of the investigated films.

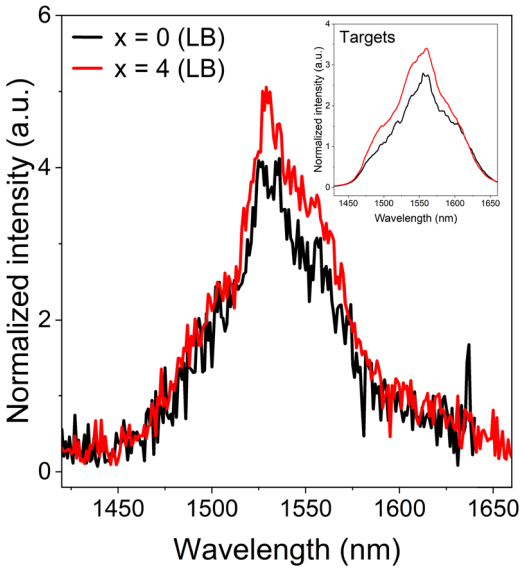

Fig. 6 NIR emission spectra normalized at 1620 nm obtained using λ_{exc} = 976 nm for the x = 0 (LB) and x = 4 (LB) films deposited on BK7. The inset shows the normalized emission spectra of the corresponding targets.

T_p (Table 1), a more polymerized network (Fig. 2(b)) and lower RIs (Fig. 2(c)) than expected. Nevertheless, the x = 4 (LB) glass exhibits similar spectroscopic properties to the x = 4 glass (Fig. 3(a), (c), (d) and Table 3), confirming that this glass is promising for amorphous thin films' deposition.

3.2 Film deposition and characterization

Amorphous films were successfully deposited from x = 4 (LB) and from x = 0 (LB) using rf-magnetron sputtering, as confirmed from the XRD patterns (shown in SI Fig. S1(b)). The absence of sharp peaks in the XRD pattern suggests that no significant crystallization took place, especially during the deposition process of the x = 4 (LB) and confirming our former study.[23] The thickness of the two films, estimated using ellipsometry data fits, is ~400 nm, showing that the deposition rate is similar for both glasses. Therefore, the presence of F in the target is not expected to influence the deposition rate. As presented in Table 4, the two films exhibit similar compositions with an increased bismuth (Bi) content and reduced tellurium (Te) concentration as compared to the targets, confirming that rf-magnetron sputtering is a viable method for depositing tellurite films, consistent with previous discussions in ref. 23. F was also detected in the x = 4 (LB) film.

The transmission spectra of the investigated films, shown in Fig. 5(a), display a high transmission value (~92%) close to that of the BK7 substrate at the maxima of the interference

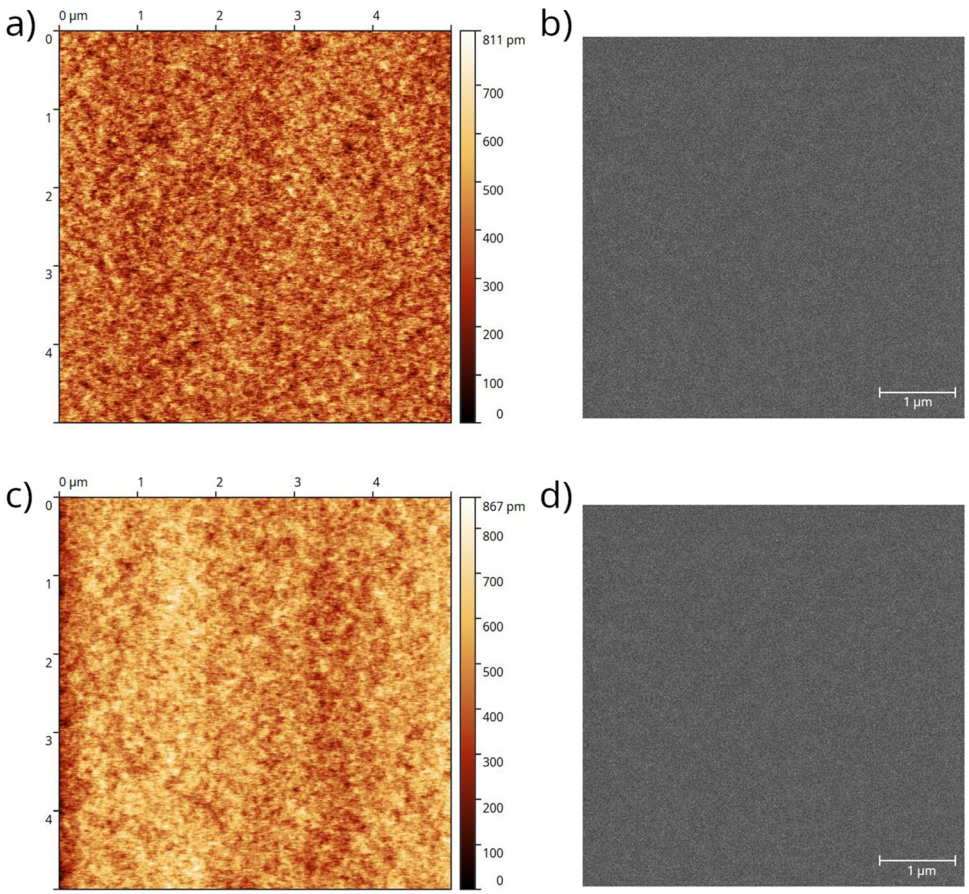

Fig. 7 Surface profiles of the x = 0 (LB) and x = 4 (LB) films measured using AFM (a and c, respectively) and using SEM (b and d, respectively).

fringes. A Tauc plot for the indirect allowed transition was generated from the transmission spectra and is shown in Fig. 5(b). Both films show a clear linear portion, confirming that the films display an indirect optical bandgap in agreement with our previous study.[23] Fig. 5(c) displays the RI dispersion curves obtained from the ellipsometry data fits. As observed for the bulk samples, the $x = 4$ (LB) film has slightly lower RIs than the $x = 0$ (LB) film due to the presence of F in the film as discussed in the previous section.

The normalized NIR emission spectra at 1620 nm of the investigated films, presented in Fig. 6, show the typical Er^{3+} 1.5 μm NIR emission originating from $^4I_{13/2} \rightarrow {}^4I_{15/2}$ transition, confirming the presence of Er^{3+} ions in the films. One should mention that the shape of the emission bands from the bulk glass targets is different from that of the films due to reabsorption of Er^{3+} occurring in the thick bulk samples, as discussed in ref. 23. Since the films were not annealed after deposition, it is believed that annealing the films would lead to an increase in the spectroscopic properties as performed in ref. 52 and 53, which would be tried out in a future work.

The surface of the investigated films was scanned using AFM. As shown in Fig. 7(a) and (c), both films exhibit a uniform surface with no voids, further supporting the absence of significant crystallization, particularly during the deposition of the F-containing glass. Both films exhibit similar low surface roughness, with a root mean square value of (0.1 ± 0.1) nm. Similar roughness values were seen for the same glass composition.[23] The surface uniformity in terms of topography was confirmed using SEM (Fig. 7(b) and (d)).

4. Conclusions

In this work, we have shown that the addition of NH_4F–HF up to 4 wt% into a tellurite glass batch before melting can effectively decrease the concentration of OH groups, leading to an enhancement in the spectroscopic properties of the glass. However, this process leads to residual F in the glass network, resulting in a change in the thermal and structural properties of the glass as well as its RI. The presence of residual F in the glass network does not affect the film deposition process carried out *via* rf-magnetron sputtering. Amorphous and transparent films with low surface roughness were successfully deposited from a glass target melted with 4 wt% of NH_4F–HF. F was detected in the film, leading to a film with slightly lower RI compared to a film deposited from an untreated glass target, consistent with the known variation of RI in bulk glasses as a function of fluorine content. Our findings are significant for the fabrication of Er^{3+} tellurite glass films deposited from targets with reduced OH content and offer promising prospects for developing integrated photonics.

Author contributions

Pradeep Ramanan: writing – review & editing, writing – original draft, methodology, formal analysis, data curation, and conceptualization. Florent Starecki: writing – review & editing, methodology, formal analysis, and data curation. Jan Gutwirth: writing – review & editing, methodology, and formal analysis. Virginie Nazabal: writing – review & editing, validation, supervision, project administration, funding acquisition, formal analysis, and conceptualization. Matthieu Roussey: writing – review & editing, methodology, and formal analysis. Petr Nemec: writing – review & editing, validation, supervision, project administration, funding acquisition, formal analysis, and conceptualization. Laeticia Petit: writing – review & editing, writing – original draft, validation, supervision, project administration, funding acquisition, formal analysis, and conceptualization.

Conflicts of interest

There are no conflicts to declare.

Data availability

All data relevant to the work have been presented in detail within the article. Additional data supporting this article have been included as part of the supplementary information (SI). Supplementary information: X-ray diffractograms and UV-VIS-NIR spectra from 750–1700 nm. See DOI: https://doi.org/10.1039/d5ma01066g.

Acknowledgements

The work leading to this publication has received funding from the European Union's Horizon Europe research and innovation program under grant agreement number 101092723/IBAIA. UK participants in Horizon Europe Project IBAIA are supported by UKRI grant number 10062902 (MODUS). The work is also supported by the Flagship on Photonics Research and Innovation (PREIN) funded by the Research Council of Finland, decision 346518 (UEF) and 320165 (TAU). The authors would like to acknowledge Dr Stanislav Slang for his discussion and guidance in materials analysis.

References

1 J. D. B. Bradley and M. Pollnau, *Laser Photonics Rev.*, 2011, **5**, 368–403, DOI: 10.1002/lpor.201000015.
2 S. Tanabe, *C. R. Chim.*, 2002, **5**, 815–824, DOI: 10.1016/S1631-0748(02)01449-2.
3 R. Bao, Z. Fang, J. Liu, Z. Liu, J. Chen, M. Wang, R. Wu, H. Zhang and Y. Cheng, *Laser Photonics Rev.*, 2025, **19**, 2400765, DOI: 10.1002/lpor.202400765.
4 Z. Chen, L. Wan, S. Gao, K. Zhu, M. Zhang, Y. Li, X. Huang and Z. Li, *J. Lightwave Technol.*, 2022, **40**, 3364–3373, DOI: 10.1109/JLT.2022.3153447.
5 Y. Liu, Z. Qiu, X. Ji, A. Lukashchuk, J. He, J. Riemensberger, M. Hafermann, R. N. Wang, J. Liu, C. Ronning and T. J. Kippenberg, *Science*, 2022, **376**, 1309–1313, DOI: 10.1126/science.abo2631.

6 T. Sakimura, K. Hirosawa, Y. Watanabe, T. Ando, S. Kameyama, K. Asaka, H. Tanaka, M. Furuta, M. Hagio, Y. Hirano, H. Inokuchi and T. Yanagisawa, *Opt. Express*, 2019, **27**, 24175–24187, DOI: 10.1364/OE.27.024175.
7 A. Lukashchuk, H. K. Yildirim, A. Bancora, G. Lihachev, Y. Liu, Z. Qiu, X. Ji, A. Voloshin, S. A. Bhave, E. Charbon and T. J. Kippenberg, *Nat. Commun.*, 2024, **15**, 3134, DOI: 10.1038/s41467-024-47478-z.
8 A. Jha, S. Shen, L. H. Huang and P. Joshi, *J. Opt.*, 2004, **33**, 157–170, DOI: 10.1007/BF03354761.
9 R. El-Mallawany, *J. Appl. Phys.*, 1992, **72**, 1774–1777, DOI: 10.1063/1.351649.
10 J. S. Wang, E. M. Vogel and E. Snitzer, *Opt. Mater.*, 1994, **3**, 187–203, DOI: 10.1016/0925-3467(94)90004-3.
11 D. L. Rhonehouse, J. Zong, D. Nguyen, R. Thapa, K. Wiersma, C. Smith and A. Chavez-Pirson, Technologies for Optical Countermeasures X; and High-Power Lasers 2013, Technology and Systems, 2013, 88980, DOI: 10.1117/12.2033925.
12 K. Richardson, D. Krol and K. Hirao, *Int. J. Appl. Glass Sci.*, 2010, **1**, 74–86, DOI: 10.1111/j.2041-1294.2010.00008.x.
13 R. Wang, X. Meng, F. Yin, Y. Feng, G. Qin and W. Qin, *Opt. Mater. Express*, 2013, **3**, 1127–1136, DOI: 10.1364/OME.3.001127.
14 D. Strakas and N. Gutknecht, *Lasers Dental Sci.*, 2018, **2**, 125–136, DOI: 10.1007/s41547-018-0036-1.
15 J. E. Stanworth, *Nature*, 1952, **169**, 581–582, DOI: 10.1038/169581b0.
16 H. A. A. Sidek, S. Rosmawati, B. Z. Azmi and A. H. Shaari, *Adv. Condens. Matter Phys.*, 2013, **2013**, 783207, DOI: 10.1155/2013/783207.
17 S. Yoshida, S. Aono, J. Matsuoka and N. Soga, *J. Ceram. Soc. Jpn.*, 2001, **109**, 753–756, DOI: 10.2109/jcersj.109.1273_753.
18 N. Effendy, S. H. Ab Aziz, H. Mohamed Kamari, M. H. Mohd Zaid and S. A. Abdul Wahab, *J. Alloys Compd.*, 2020, **835**, 155350, DOI: 10.1016/j.jallcom.2020.155350.
19 X. Shen, Y. Zhu, Y. Zhou and J. Li, *J. Opt. Soc. Am. B*, 2020, **37**, 320–328, DOI: 10.1364/JOSAB.379743.
20 E. Blessy Kamalam and N. Manikandan, *ECS J. Solid State Sci. Technol.*, 2023, **12**, 076007, DOI: 10.1149/2162-8777/ace6d8.
21 W. L. Fong, K. A. Bashar, S. O. Baki, M. H. M. Zaid, B. T. Goh and M. A. Mahdi, *J. Non-Cryst. Solids*, 2021, **555**, 120621, DOI: 10.1016/j.jnoncrysol.2020.120621.
22 A. Lemiere, B. Bondzior, I. Aromäki and L. Petit, *J. Am. Ceram. Soc.*, 2022, **105**, 7186–7195, DOI: 10.1111/jace.18649.
23 P. Ramanan, J. Gutwirth, S. Slang, A. Viswanathan, T. Ghanawi, F. Starecki, V. Nazabal, M. Roussey, P. Němec and L. Petit, *J. Am. Ceram. Soc.*, 2025, **108**, e20589, DOI: 10.1111/jace.20589.
24 R. F. Bartholomew, B. L. Butler, H. L. Hoover and C. K. Wu, *J. Am. Ceram. Soc.*, 1980, **63**, 481–485, DOI: 10.1111/j.1151-2916.1980.tb10748.x.
25 Y. Yan, A. J. Faber and H. de Waal, *J. Non-Cryst. Solids*, 1995, **181**, 283–290, DOI: 10.1016/S0022-3093(94)00528-1.
26 P. Joshi, B. Richards and A. Jha, *J. Mater. Res.*, 2013, **28**, 3226–3233, DOI: 10.1557/jmr.2013.341.
27 A. Miguel, R. Morea, M. A. Arriandiaga, M. Hernandez, F. J. Ferrer, C. Domingo, J. M. Fernandez-Navarro, J. Gonzalo, J. Fernandez and R. Balda, *J. Eur. Ceram. Soc.*, 2014, **34**, 3959–3968, DOI: 10.1016/j.jeurceramsoc.2014.05.001.
28 J. Massera, A. Haldeman, J. Jackson, C. Rivero-Baleine, L. Petit and K. Richardson, *J. Am. Ceram. Soc.*, 2011, **94**, 130–136, DOI: 10.1111/j.1551-2916.2010.04031.x.
29 A. S. Ferlauto, G. M. Ferreira, J. M. Pearce, C. R. Wronski, R. W. Collins, X. Deng and G. Ganguly, *J. Appl. Phys.*, 2002, **92**, 2424–2436, DOI: 10.1063/1.1497462.
30 K. E. Peiponen and E. M. Vartiainen, *Phys. Rev. B: Condens. Matter Mater. Phys.*, 1991, **44**, 8301–8303, DOI: 10.1103/PhysRevB.44.8301.
31 D. De Sousa Meneses, M. Malki and P. Echegut, *J. Non-Cryst. Solids*, 2006, **352**, 769–776, DOI: 10.1016/j.jnoncrysol.2006.02.004.
32 G. Guery, T. Cardinal, A. Fargues, V. Rodriguez, M. Dussauze, D. Cavagnat, P. Thomas, J. Cornette, P. Wachtel, J. D. Musgraves and K. Richardson, *Int. J. Appl. Glass Sci.*, 2014, **5**, 178–184, DOI: 10.1111/ijag.12044.
33 V. Nazabal, S. Todoroki, A. Nukui, T. Matsumoto, S. Suehara, T. Hondo, T. Araki, S. Inoue, C. Rivero and T. Cardinal, *J. Non-Cryst. Solids*, 2003, **325**, 85–102, DOI: 10.1016/S0022-3093(03)00313-2.
34 K. Li, L. Zhang, Y. Yuan and W. Wei, *Appl. Phys. B*, 2016, **122**, 85, DOI: 10.1007/s00340-016-6358-3.
35 C. Pereira, F. C. Cassanjes, J. S. Barbosa, R. R. Gonçalves, S. J. L. Ribeiro and G. Poirier, *J. Non-Cryst. Solids*, 2017, **463**, 158–162, DOI: 10.1016/j.jnoncrysol.2017.02.021.
36 T. Sekiya, N. Mochida, A. Ohtsuka and M. Tonokawa, *J. Non-Cryst. Solids*, 1992, **144**, 128–144, DOI: 10.1016/S0022-3093(05)80393-X.
37 N. Manikandan, A. Ryasnyanskiy and J. Toulouse, *J. Non-Cryst. Solids*, 2012, **358**, 947–951, DOI: 10.1016/j.jnoncrysol.2012.01.003.
38 S. X. Shen and A. Jha, *Adv. Mater. Res.*, 2008, **39–40**, 159–164, DOI: 10.4028/www.scientific.net/AMR.39-40.159.
39 A. K. Yadav and P. Singh, *RSC Adv.*, 2015, **5**, 67583–67609, DOI: 10.1039/C5RA13043C.
40 M. Evrard, T. Combes, A. Maldonado, F. Désévédavy, G. Gadret, C. Strutynski, J. C. Jules, C. H. Brachais and F. Smektala, *Opt. Mater. Express*, 2022, **12**, 136–152, DOI: 10.1364/OME.438588.
41 M. D. O'Donnell, C. A. Miller, D. Furniss, V. K. Tikhomirov and A. B. Seddon, *J. Non-Cryst. Solids*, 2003, **331**, 48–57, DOI: 10.1016/j.jnoncrysol.2003.08.081.
42 G. H. Dieke and H. M. Crosswhite, *Appl. Opt.*, 1963, **2**, 675–686, DOI: 10.1364/AO.2.000675.
43 P. Nandi and G. Jose, *Opt. Commun.*, 2006, **265**, 588–593, DOI: 10.1016/j.optcom.2006.03.045.
44 I. Jlassi, H. Elhouichet, M. Ferid, R. Chtourou and M. Oueslati, *Opt. Mater.*, 2010, **32**, 743–747, DOI: 10.1016/j.optmat.2010.02.006.
45 E. S. Yousef, *J. Alloys Compd.*, 2013, **561**, 234–240, DOI: 10.1016/j.jallcom.2013.01.199.
46 M. S. Sajna, S. Thomas, C. Jayakrishnan, C. Joseph, P. R. Biju and N. V. Unnikrishnan, *Spectrochim. Acta, Part A*, 2016, **161**, 130–137, DOI: 10.1016/j.saa.2016.02.039.
47 X. Feng, S. Tanabe and T. Hanada, *J. Non-Cryst. Solids*, 2001, **281**, 48–54, DOI: 10.1016/S0022-3093(00)00429-4.

48 S. N. Nazrin, M. S. Sutrisno, H. B. Zaman, N. Jothi, A. Assaiqeli and S. Ezzine, *J. Lumin.*, 2025, **281**, 121184, DOI: 10.1016/j.jlumin.2025.121184.
49 M. Caetano, J. C. S. Filho, R. F. Moraes, A. A. Andrade, A. C. A. Silva and N. O. Dantas, *Braz. J. Phys.*, 2020, **50**, 410–418, DOI: 10.1007/s13538-020-00754-x.
50 L. Gomes, M. Oermann, H. Ebendorff-Heidepriem, D. Ottaway, T. Monro, A. Felipe Henriques Librantz and S. D. Jackson, *J. Appl. Phys.*, 2011, **110**, 083111, DOI: 10.1063/1.3651399.
51 L. Gomes, D. Rhonehouse, D. T. Nguyen, J. Zong, A. Chavez-Pirson and S. D. Jackson, *Opt. Mater.*, 2015, **50**, 268–274, DOI: 10.1016/j.optmat.2015.11.007.
52 V. Nazabal, A. M. Jurdyc, P. Němec, M. L. Brandily-Anne, L. Petit, K. Richardson, P. Vinatier, C. Bousquet, T. Cardinal, S. Pechev and J. L. Adam, *Opt. Mater.*, 2010, **33**, 220–226, DOI: 10.1016/j.optmat.2010.08.023.
53 J. Fick, É. J. Knystautas, A. Villeneuve, F. Schiettekatte, S. Roorda and K. A. Richardson, *J. Non-Cryst. Solids*, 2000, **272**, 200–208, DOI: 10.1016/S0022-3093(00)00119-8.